Mass timber seismic lateral force resisting systems: Testing of a full-scale three-story structure

Arijit Sinha *†
Professor and JELD-WEN Chair of Wood-based Composites Science,
Department of Wood Science and Engineering, Oregon State University, Corvallis, OR 97331
Email: Arijit.sinha@oregonstate.edu

Andre R. Barbosa
Cecil and Sally Drinkward Professor in Structural Engineering, School of Civil and Construction Engineering,
Oregon State University, Corvallis, OR 97331
Email: andre.barbosa@oregonstate.edu

Tu X. Ho
Associate Engineer R&D, Simpson Strong-Tie, Pleasanton, CA 94588
Email: tuho@strongtie.com

Barbara G. Simpson
Assistant Professor, Department of Civil and Environmental Engineering,
Stanford University, Stanford, CA Email: Bsimpson@stanford.edu

Gustavo Araujo
Graduate Research Assistant, Stanford University, Stanford, CA 94305
Email: garaujor@stanford.edu

Byrne T. Miyamoto †
Former Research Manager, Tallwood Design Institute,
Corvallis, OR 97331 Email: Byrne.Miyamoto@oregonstate.edu

Patricio Uarac
Postdoctoral Scholar, Department of Wood Science and Engineering,
Oregon State University, Corvallis, OR 97331 Email: Patricio.Uarac@oregonstate.edu

Gustavo F.O. Orozco
Senior Project Engineer, Thornton Tomasetti, Washington, DC 20036
Email: gusorozco11@gmail.com

(Received 14 January 2026)

Abstract: Over the last decade, the North American market for mass timber (MT) has diversified with the development of several engineered wood panelized products. Among these, a recent veneer-based product known as mass ply panel (MPP) has been introduced and certified per ANSI-PRG 320. To further demonstrate the potential of such engineered wood panelized products, a study was conducted to develop innovative solutions for enhanced design to low-damage seismic lateral force-resisting systems (LFRS). This paper presents an overview of the study, in which a three-story MT building was designed following performance-based design methods and constructed at Oregon State University (OSU). The gravity system includes laminated veneer lumber beams and columns and MPP floors. Two different LFRS for balloon-type MPP shear walls were studied. The first LFRS consisted of a pivoting MPP panel with steel buckling-restrained boundary elements (BRB) as energy dissipators. The second system utilized a rocking MPP panel with post-tensioned steel rods to provide self-centering capacity and U-shaped flexural plates (UFP) to dissipate energy. There were four testing phases, including two phases (Phases 0.1 and 0.2) that applied lateral loads to the gravity system only, before and after testing of LFRS; Phase 1, which included lateral testing of the building structure with an BRB-MPP shear wall; and Phase 2, which included lateral testing of the building structure with an UFP-MPP shear wall. In all four phases, the building was subjected to quasi-static cyclic tests following a CUREE protocol up to maximum 4% roof lateral drift. A summary of building details, experimental setup and key results is presented in this paper.

Keywords: Buckling restrained braces; CUREE; Earthquake engineering; Lateral force-resisting system; Mass timber; Mass ply panel; Performance-based design; Quasi-static cyclic test; U-shaped flexural plates.

---

* Corresponding author
† Society of Wood Science & Technology member

Wood and Fiber Science, 58(3), 2026, pp. 197–215.
https://doi.org/10.22382/wfs-2026-18

Introduction

Mass timber (MT) buildings have experienced a surge in popularity in recent years, as is evident through successful projects employing exclusively mass timber structures or incorporating various mass timber components alongside steel and concrete systems (Kılınç 2025; Fernandez et al. 2020; Liven and Abrahamsen 2023). Ongoing advancements in research and technology are enhancing the seismic resilience of mass timber buildings. In line with efforts to design structures that withstand strong ground shaking with minimal damage, numerous tests have been conducted to assess the structural performance of mass timber buildings. One noteworthy example of a low-damage lateral force resisting system (LFRS) is the self-centering rocking wall system. This innovative system comprises a rigid, primarily elastic wall element, post-tensioning rods, and energy dissipation devices (Granello et al. 2020).

To assess the performance of self-centering rocking wall systems employing cross-laminated timber (CLT), a two-story mass timber building underwent testing at the University of California San Diego (UCSD) National Science Foundation's Natural Hazards Engineering Research Infrastructure (NHERI) shake-table facility in 2017 (Blomgren et al. 2019; Mugabo et al. 2021; Pei et al. 2019). Furthermore, a comprehensive body of literature documents component tests focused on self-centering rocking wall systems utilizing mass timber elements (Araújo R. et al. 2025; Brown et al. 2021; Ganey et al. 2017; van de Lindt et al. 2019; Pei et al. 2024; Sarti et al. 2015, 2016; Uarac et al. 2025). With the continuous production and certification of new mass timber panels (MTPs) and the introduction of additional designs for seismic force-resisting systems, there are increased opportunities for the development of innovative LFRS.

This paper summarizes a multi-phase research project that includes construction of a full-scale three-story building structure specimen designed to test two different LFRS. There were four testing phases, including two phases (Phases 0.1 and Phase 0.2) that applied lateral loads to the gravity system only, before and after testing of LFRS. In Phase 1, lateral loads were transferred through mass ply panel (MPP) diaphragms to an LRFS consisting of an MPP spine with vertically oriented energy-dissipating buckling-restrained braces (BRBs) in the first story. In Phase 2, the LFRS consists of an MPP, post-tensioning rods connecting the top of the panel to the foundation, and U-shaped flexural plates (UFPs) that provide energy dissipation capability. These UFPs are attached between the MPP and boundary steel columns (designed to remain essentially elastic) that connect to the foundation. In both Phase 1 and 2, the LFRS is connected to the diaphragms of a mass timber gravity system, consisting of MPP floor slabs and laminated veneer lumber (LVL) beams and columns. The gravity connections were designed to remain damage free up to approximately 5% of inter-story drift ratio. The connection between the LFRS and the diaphragms only allows for transfer of lateral loads between the MPP wall and floor panels, so the rocking mechanism is not affected by the gravity system (Barbosa et al. 2021; Blomgren et al. 2019; Mugabo et al. 2021). The design includes force-based design procedures for the gravity system, and displacement- and performance-based seismic design procedures for the LFRS. Additionally, drift and force capacity design checks were performed for various components of the gravity system and connections.

The aim of the test program presented in this paper was to investigate the behavior of a full-scale three-story mass-timber building system equipped with two different LFRS, consisting of an MPP spine and a resilient rocking wall. The intention was to validate the design process and replicate the construction details required for practical implementation. The specific objective was to estimate the global load-displacement behavior and displacement capacity of the two different systems. Additionally, the test was conducted to evaluate the structural system's resilience by subjecting it to significantly high drift levels, surpassing the limits required by current building codes, thus examining and validating its robustness.

This study is part of larger experimental campaign on innovative lateral systems employing mass timber as part of the Emmerson Lab Launch Initiative (ELLI). An overview of the experimental campaign and notable results is presented in this paper. Detailed results and calibrated numerical models from different phases of ELLI can be found in (Araújo et al. 2025; Uarac et al. 2025).

Materials and methods

Design requirements

The test building represents a portion of an 18.3 m (60 ft) by 30 m (100 ft) three-story office archetype building located in Seattle, WA (47.582 N, 122.331 W), site class D (S_{DS} = 0.97 g, S_{D1} = 0.61g). Design gravity loads consisted of dead loads of 2.87 kPa (60 psf) for the second and third floor levels and 2.63 kPa (55 psf) for the roof. Live loads considered were 3.11 kPa (65 psf) for the floor levels and 0.96 kPa (20 psf) for the roof. The total seismic weight included in the seismic design was

5,289 kN (1,189 kips), which was evenly distributed over six shear walls (in each loading direction) of the office building archetype. Note that the seismic weight did include live load per ASCE 7-16 (ASCE/SEI 2017).

For the seismic design, three hazard levels were considered in the overall project: (1) service level earthquake (SLE); (2) design earthquake (DE); and (3) risk-targeted maximum considered earthquake (MCE_R). However, in the design of the two different LFRS, these limits were applied differently. The pivoting mass timber-steel BRB system utilized only the DE and MCE_R drift targets, adopting story drift ratio limits of 2% per ASCE 7-16 (Table 12.12-1) and scaled by 3/2 (3%) for the MCE_R level (Araújo et al. 2025). The post-tensioned UFP wall system employed the same DE and MCE_R drift limits and additionally incorporated an SLE drift target of 0.5% to limit nonstructural damage (Uarac et al. 2025). Additional performance expectations were defined for three hazard levels (SLE, DE, and MCE_R) and are presented in the following sections for both the LFRS employed.

Gravity framing

The overall footprint of the test building was 12.19 m × 12.19 m (40 × 40 ft) (Figure 1). The first story height was 3.15 m (10 ft 4 in.) from the top of foundation beams to the top of floor, and the height of second and third stories was 2.74 m (9 ft), leading to a total building height of 8.64 m (28 ft 4 in.). The gravity system was designed symmetrically to create a two-bay by two-bay configuration. There were 12 LVL columns (178 mm × 178 mm (7 in. × 7 in.) total in each story. LVL beams, with cross-section of 133 mm × 559 mm (5.25 in. × 22 in.) spanned column axis to column axis in the north-south direction. In the first story, columns rested on LVL foundation beams with a combined cross-section of 356 mm × 356 mm (14 in. × 14 in.). Beams and columns consisted of Douglas-fir 2.1E 3100 and 1.8E 2650 rated LVL (ICC and APA 2025), respectively. The spacing between adjacent collar beams along the building centerline in the loading direction was 490 mm (1 ft 7-1/4 in.), providing sufficient clearance between beams to accommodate the shear walls.

The beam-to-column and column-to-foundation-beam connections were steel column caps (Figure 2a and Figure 2b, respectively) were custom made and allowed rocking at the beam-to-column interface to accommodate large, up to 5%, inter-story drift ratios of the building. This connector design, which is like the one utilized by Pei et al. (2019), adopts vertical slotted bolt holes to minimize moment transfer and damage to the joints. In the east-west direction, a steel angle member was added to each beam-to-column connection to enhance out-of-plane stability of the beam (Figure 2a).

Diaphragm

The diaphragm at each floor level consisted of twelve 181 mm (7-1/4 in.) thick MPP panels, which spanned in the east-west direction, i.e., perpendicular to the loading direction and fixed to LVL beams with SDCP 221100 screws (ICC 2025) spaced at 305 mm (12 in.) on-center (Figure 2c). Adjacent diaphragm panels were connected by 149 mm (5-7/8 in.) wide spline connections of 19 mm (3/4 in.) thick plywood and two rows of SDCP 22434 screws (ICC 2025) (Figure 2d). The diaphragm was designed to remain essentially elastic for the various phases of this project. The lateral loads used for diaphragm design were determined following both the traditional and alternative design methodologies described in Chapter 12 of ASCE 7-16 (ASCE/SEI 2017), and in accordance with the SDPWS 2021 (AWC/ANSI 2020) for diaphragm shear force.

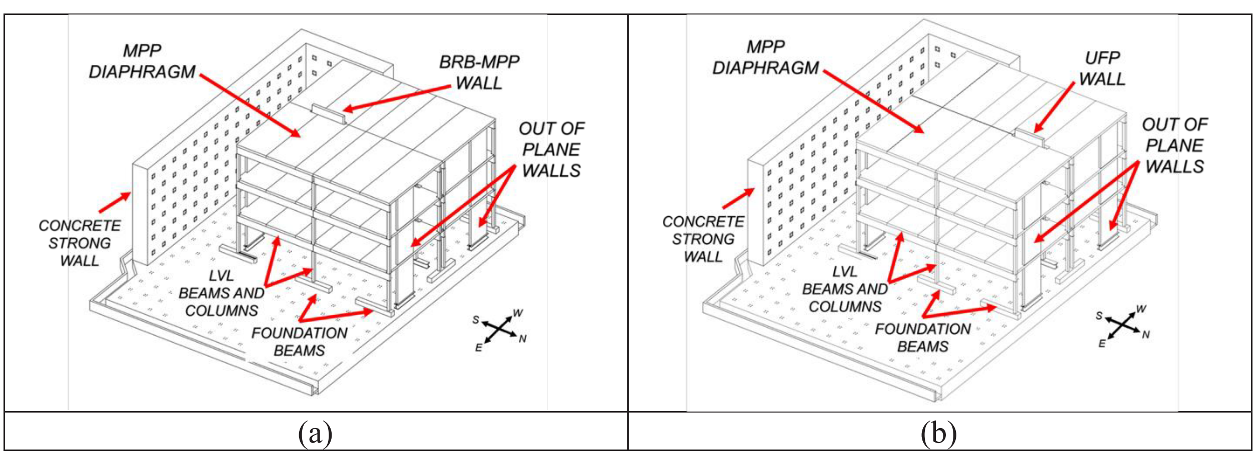

Figure 1. Three-dimensional view of test building: (a) Phase 1 – pivoting mass timber-steel BRB system; (b) Phase 2 – post-tensioned UFP wall.

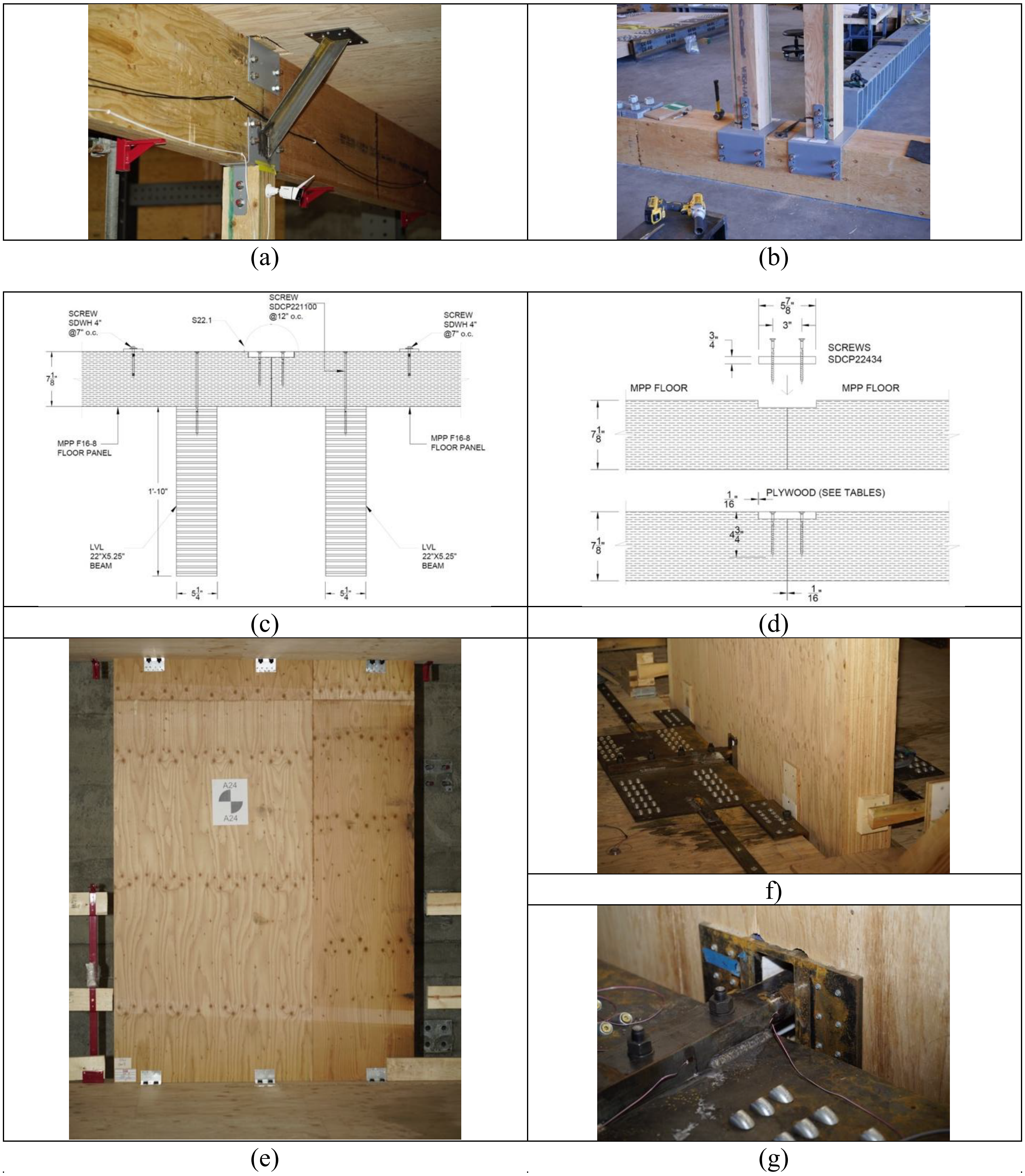

Figure 2. Building connection details: (a) beam-to-column connection; (b) column-to-foundation connection; (c) diaphragm-to-beam connection; (d) diaphragm spline connection; (e) out-of-plane wall connection; (f) shear transfer mechanism; and (g) steel window, shear key, wing plate and shear collector.

Out-of-plane walls

Four platform-type out-of-plane shear walls were placed at each story perpendicular to the applied loading direction to improve the torsional stability of the building (see Figure 1). Each out-of-plane wall was 127 mm (5 in.) thick, 1.83 m (6 ft) wide MPP panel connected to top and bottom diaphragm panels using A3 connectors (Amini et al. 2018; AWC/ANSI 2021) (Figure 2e). Because lateral loading during testing was applied only in the north-south direction, these out-of-plane walls were designed to resist up to 10% of the estimated north-south capacity.

Wall-to-diaphragm connections

At each floor level, the lateral load was transferred from diaphragm to the shear wall through a slotted shear transfer mechanism (i.e., shear wall-to-diaphragm connection) consisting of a shear key attached to the panels and wing plates (Figure 2f). The design of wall-to-diaphragm connection was based on the connection design in the two-story building shake table test (Blomgren et al. 2019; Pei et al. 2019) with some modifications, including a two-sided load transfer, unlike the shake table testing, and where welding was added between the shear key and wing plate to increase the strength and effective stiffness of the connection. This design allows transferring effectively shear force from the diaphragms to the shear walls and constraining out-of-plane movement of the shear walls, while allowing uplift of the wall panel relative to the diaphragms. At each floor level, a steel window was inserted into a prefabricated cut-out on the MPP wall panel. A shear key was assembled through the window. The segment of shear key, which contacted with the steel window, was rounded at its four corners. In addition, low friction PTFE plates were glued to the inside faces of steel windows. These details allow smooth relative movement between shear keys and steel windows when the wall uplifted (Figure 2g). To transfer lateral load from diaphragm to the shear wall, each shear key was connected to one steel wing plate on each side of the shear wall by a combination of four 3/4 in. diameter tension-controlled bolts and weld connections. Each wing plate was attached to the floor panels by 60 inclined SDCF 22858 screws (ICC 2025). Shear collectors, including two steel plate segments on each side of shear wall, ran across diaphragm panels in a north-south direction and were tied down to diaphragm panels by SDWH 27400G screws (IAPMO 2025) spaced at 178 mm (7 in.) on-center and welded to wing plates for collecting and transferring lateral loads from the diaphragm panels to wing plates.

Pivoting mass timber-steel BRB system

The first LFRS included a hybrid of a 9144 mm × 2515 mm × 203 mm (30 ft × 8 ft-3 in. × 8 in.) MPP shear wall and two BRBs attached to the shear wall ends as hold-downs at the first story level, herein referred to as the hybrid BRB-MPP spine, essentially acting as stiff backbone to the structure. The BRBs were designed to entirely resist the base moment, while the MPP wall resisted the story shear. This BRB-MPP spine wall was conceived as a pivoting wall with a pin support located at the base midpoint to allow the wall to jointly pivot (Figure 3a). Shear transfer to the foundation was ensured by using two stiff steel shear key assemblies, designed as slip-critical connections to the steel foundation beam. These assemblies prevented in-plane sliding and restrained out-of-plane displacement of the wall relative to the foundation (Figure 3b).

The design base shear, V_b, was estimated using the DE spectrum from ASCE 7-16 and a response modification factor of R = 8, consistent with BRB-frame systems (ASCE 7-16 [ASCE/SEI 2017] Table 12.2-1, item 25). The base shear was distributed at each floor level as equivalent static lateral forces based on the first-mode shape. Because the BRBs were intended to yield primarily under first-mode overturning demands, the MPP spine was proportioned to remain essentially elastic (Araújo et al. 2025). As discussed in that work, yielding of the BRBs does not limit higher-mode inertial forces, which can generate additional story shear demands beyond those associated with first-mode behavior. Therefore, the dimensions of the MPP panel were also verified for near-elastic story shears resulting from these higher-mode contributions to ensure the intended elastic response of the spine under all modes of excitation.

Strain demands in the yielding core of the BRBs were also limited to the minimum between 2.5% and 10 times the steel's yield strain at the MCER level to mitigate fracture in tension. The spine components (i.e., the MPP wall and BRB-MPP connections) were capacity designed for the expected force demands at a target story drift ratio of 4% to achieve enhanced performance at intensities higher than the risk-targeted maximum considered earthquake (MCER).

The connections at the ends of the BRBs were designed to transfer the tensile and compressive forces delivered by the BRBs. The connection plates incorporated horizontal slotted holes and custom slotted washers, a configuration that provided high axial stiffness, while allowing the required relative motion (Araújo et al. 2025). This detail ensured reliable force transfer without restricting the rotation of the BRB-MPP spine. The selected BRB-to-MPP connection assembly included two 10-mm (3/8-in) side plates connected to the MPP through screws inclined at a 45° angle. The side plates were connected to a 38-mm (1.25-in.) thick base plate (termed "bottom plate" in Figure 3b), which ultimately connected to a 19-mm (0.75-in.) thick gusset plate, forming a T-shaped connection. The gusset plate was bolted to the ends of the BRBs (termed as "BRB lugs" in Figure 3b). The provided detail takes advantage of the high strength and stiffness of inclined screws in tension, while compressive forces are transferred through the bearing of the MPP on the bottom plate. To promote contact between the MPP and the bottom plate, 10 SDCF27400 (ICC 2025) self-driving screws oriented upwards were added to the con-

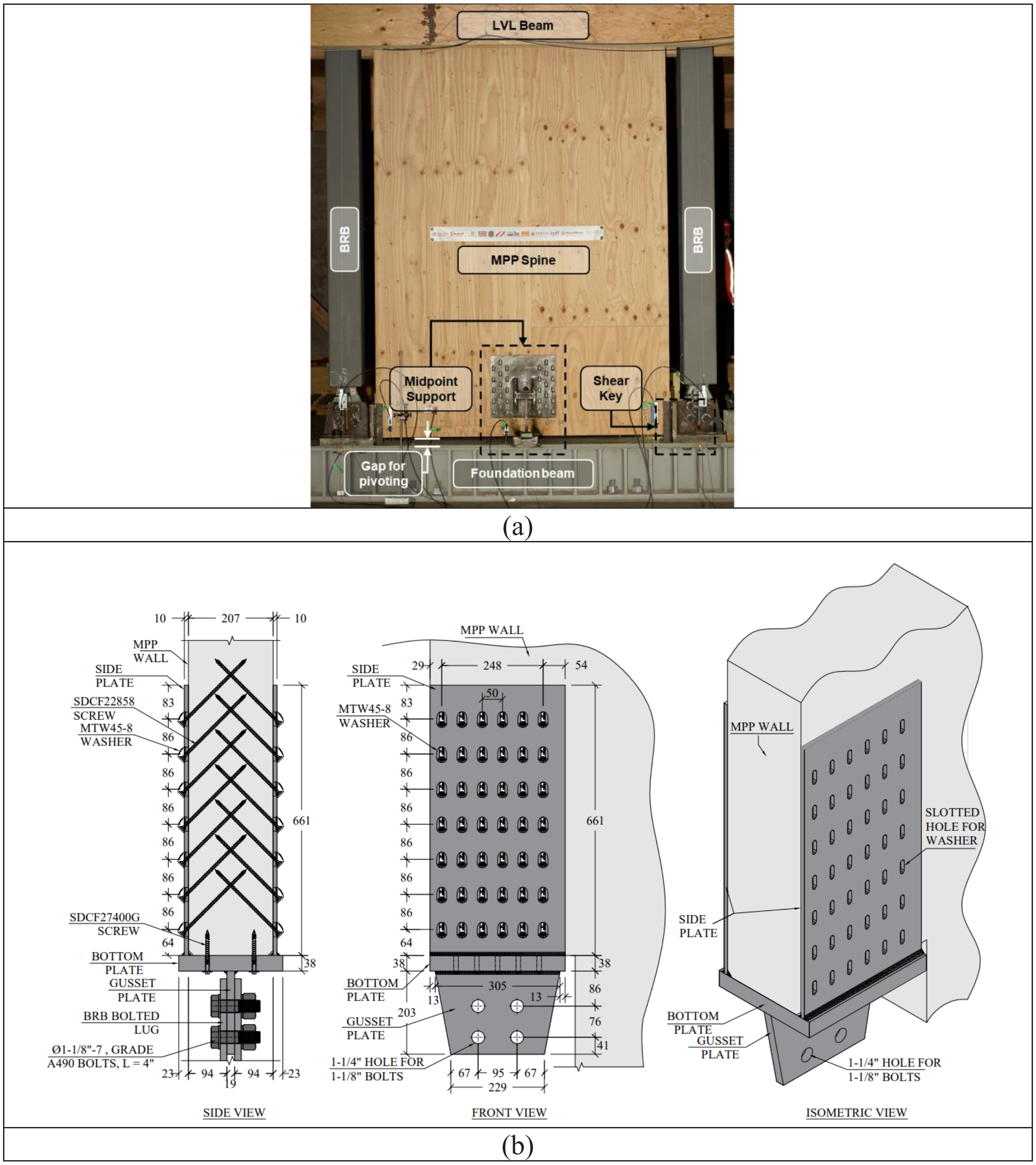

Figure 3. Pivoting spine: (a) close-up view at the first story; and (b) BRB to MPP connection details. Note: Measurements in mm; 1 in = 25.4 mm.

nection. The connection was checked against wood block shear and net rupture, compression bearing, and fastener strength in accordance with NDS (AWC 2018).

Post-tensioned UFP wall

A balloon-type MPP shear wall 9144 × 2134 × 181 mm (30 ft × 7 ft × 7 in.) was combined with four external post-tensioning high-strength rods [ASTM A354 Grade BD (ASTM 2017); diameter of 31.8 mm (1-1/4 in.), f_{pu} = 1,034 MPa (150 ksi) and f_{py} = 896 MPa (130 ksi)] to provide the self-centering capacity through rocking behavior (Figure 4a), herein referred as the "UFP post-tensioned rocking wall" or "UFP wall" in short. The high-strength rods were post-tensioned to an initial force of 151 kN (34 kip). The rods were anchored to steel saddles at the top of the MPP wall (Figure 4b) and to steel plates welded to the top flange of the foundation beam (Figure 4c). At the first-story level, the UFP wall was connected to a steel column (C10x25) at each end using UFPs, which would dis-

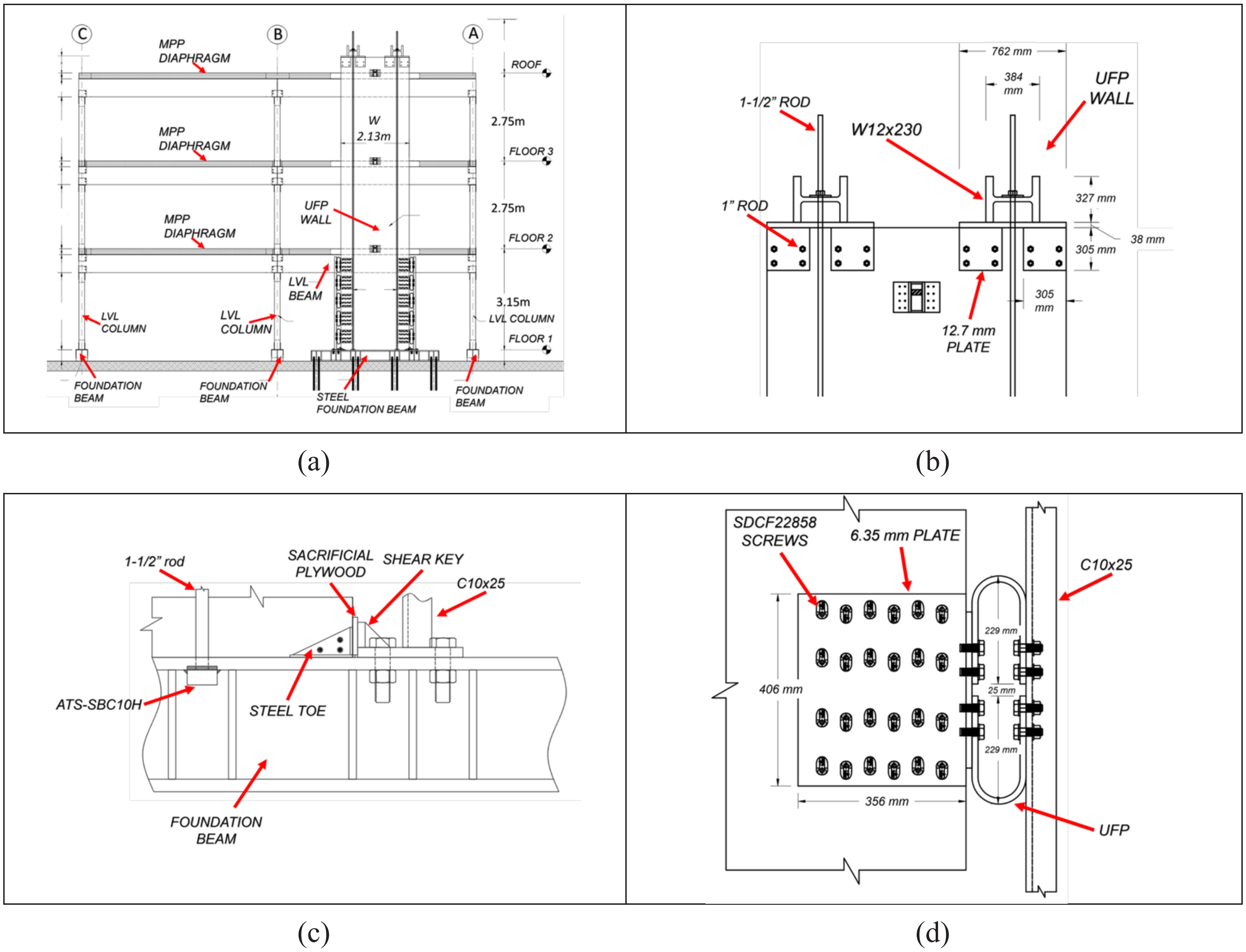

Figure 4. (a) Elevation view of test building with rocking wall; (b) steel anchor saddle at top of MPP wall; (c) steel anchor plate welded to foundation steel beam, shear key and steel toe details; and (d) UFP connection details.

sipate energy during a seismic event (Figure 4c). There were 20 UFPs [ASTM A572 Grade 42 (ASTM 2021); width of 152 mm (6 in.); thickness of 12.7mm (0.5 in.); and bending diameter of 102 mm (4 in)]. To prevent the sliding movement of the rocking wall, two foundation shear keys were designed and integrated to the base plates of steel columns, which were bolted to the steel foundation beam (Figure 4c). A gap of 13 mm (0.5 in.) was left between a shear key and each end of the wall and was filled by a sacrificial plywood piece to prevent the crushing of MPP in a minor, perpendicular-to-the-surface direction. In addition, a steel toe was included at each bottom corner of the rocking wall to reduce the crushing of MPP in a major direction at the rocking interface.

The UFPs were anchored to the wall through a welded connector assembly comprising two plates bearing against the wall faces and a third plate at the wall edge. These three plates formed a U-shaped bracket that provided the seat for attaching the UFPs as shown in the Figure 4d. Inclined SDCF 22858 screws (ICC 2025) were used for U-shaped bracket-MPP wall connection, while 5/8 in. A325 bolts (ASTM 2025) were used for UFPs-steel column and UFPs-U-shaped bracket connections.

The performance-based design procedure for the UFP rocking wall LFRS was based on the direct displacement-based design (DDBD) procedure (Di Cesare et al. 2019; Pang et al. 2010) and utilized a flag shape hysteretic model (Nakaki et al. 1999; Priestley and Grant 2005) to estimate the effective, equivalent viscous damping for the whole wall system. For the DE level, an effective damping ratio of 10.36% was adopted, following the procedure described in Uarac et al. (2025). The design base shear was estimated using the capacity spectrum approach (Pang et al. 2010), assuming an inverted-triangular displacement shape for the system (Newcombe 2011; Priestley et al. 2007). Strength design was used to select the shear wall component dimensions, number of UFPs and rods, and other design parameters. The moment capacity of the shear wall and stresses in the post-tensioned rods and MPP were checked by an analytical procedure based on the Modified Monolithic Beam Analogy (MMBA) (Palermo et al. 2004; Uarac et al. 2025). In this approach, a nonlinear finite-element model was not needed during this design stage.

There are three performance levels corresponding to three hazard levels (SLE, DE, and MCER) considered in the design. Beside the peak inter-story drift (which was discussed in the Design requirements section), the stresses and strains of the post-tensioning rods and MPP are additional design criteria for each performance level. The strains in the post-tensioning rods and MPP were limited to the elastic range at the SLE and DE levels, but were allowed to yield at the MCER level. For the MPP, an elastic-plastic model was assumed, with a yield stress of 43.01MPa (6.23 ksi), yield strain of 0.0032 (DE limit), and ultimate strain of 0.0075 (MCER limit), based on results in Soti et al. (2021). The high-strength rods were assigned a yield strain of 0.0065, using a 0.2% offset from the elastic limit (ASTM 2017). The ultimate strain of 0.085 was taken from Ocel and Provines (2015).

Test building construction

The construction of the test building proceeded in several coordinated stages to integrate the gravity framing, diaphragm system, and the different LFRS used across the testing phases. Construction began with the installation of the building foundations to the strong floor. Steel beams were placed as foundation elements beneath the LFRS and the out-of-plane walls, while LVL beams were used as foundations beneath the gravity-system columns. With the foundation system in place, the out-of-plane walls, the LVL gravity framing, and some diaphragm panels of the first story were assembled. After the first-floor gravity system was erected, both LFRS, each installed with its respective energy-dissipation system (BRBs and the UFPs), were positioned in place but intentionally left unconnected to the diaphragm panels. This allowed the remaining floor panels and all diaphragm hardware to be installed without interference, and enabled the uninterrupted erection of the gravity system for the upper stories.

After installation of each lateral system, the remaining stories were erected, following the same sequence of installing LVL columns, out-of-plane walls, beams, and diaphragm panels. This repeated procedure ensured consistent construction, detailing, and boundary conditions across all testing phases.

For each of the four testing phases, the corresponding lateral system was then connected to the diaphragm. In Phases 0.1 and 0.2, no wall was attached, in order to evaluate the gravity system response in isolation. In Phase 1, the pivoting mass timber-steel BRB system was connected, using the shear-transfer mechanism described previously. For Phase 2, the BRB wall remained in place but was left disconnected from the diaphragms, while the post-tensioned UFP wall was attached instead to evaluate the self-centering system.

Quasi-static building test

Test setup and loading protocol

Three actuators, which reacted against a 7.6 m (25-ft) tall by 18.3 m (60-ft) long strong wall, were attached to diaphragms to apply the load to the building. The loading direction, which is parallel to the investigated LFRS, is in the north-south (N-S) direction shown in Figure 1. A quasi-static cyclic displacement control-loading protocol (Figure 5) was used, which followed an abbreviated version of the CUREE protocol (Krawinkler et al. 2000). The displacement in the CUREE protocol was based on the actual building roof movement measured by the string pot at the wall line. The top actuator worked as a primary actuator and was set to displacement control, while two lower hydraulic actuators were set as secondary (follower) actuators and were set to force-based mode, following the primary actuator. The loading rate of 40.6 mm/min (1.6 in/min) was utilized for the primary actuator at the initial small cycles up to 0.4% drift. Then, the loading rate was reduced to 20.3 mm/min (0.8 in/min) for displacement cycles larger than 0.4%. The system of

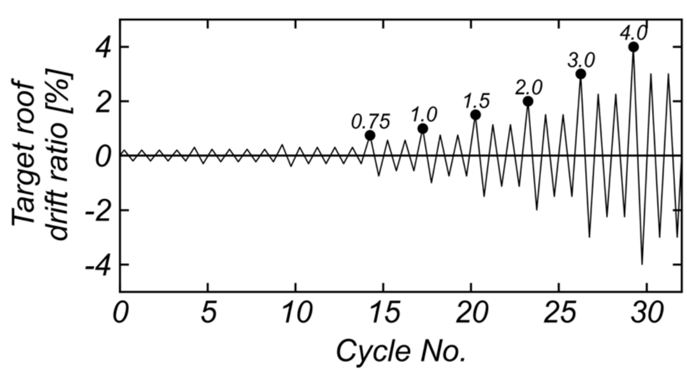

Figure 5. Abbreviated CUREE protocol utilized in the quasi-static cyclic test.

three actuators created a triangular force profile applying to the building and being proportional to the elevation of the actuators. The force feedback from the primary actuator was used to determine the force commands for the secondary actuators, such that the actuator at the first and second story were set to 0.357 and 0.679 times the primary actuator force, respectively. The load from actuators was transferred through steel loading beam to diaphragm panels on both sides of the shear wall line.

Instrumentation

The lateral loads applied to the test building were measured using load cells attached to the hydraulic actuators. The real-time reading data from central string potentiometers at roof level (SP11) was utilized to control the primary actuator movement following the loading protocol (Figure 6a). In addition, at each floor level, there was one string potentiometer connected between walls (SP1, SP5, SP9, Figure 6a) to record

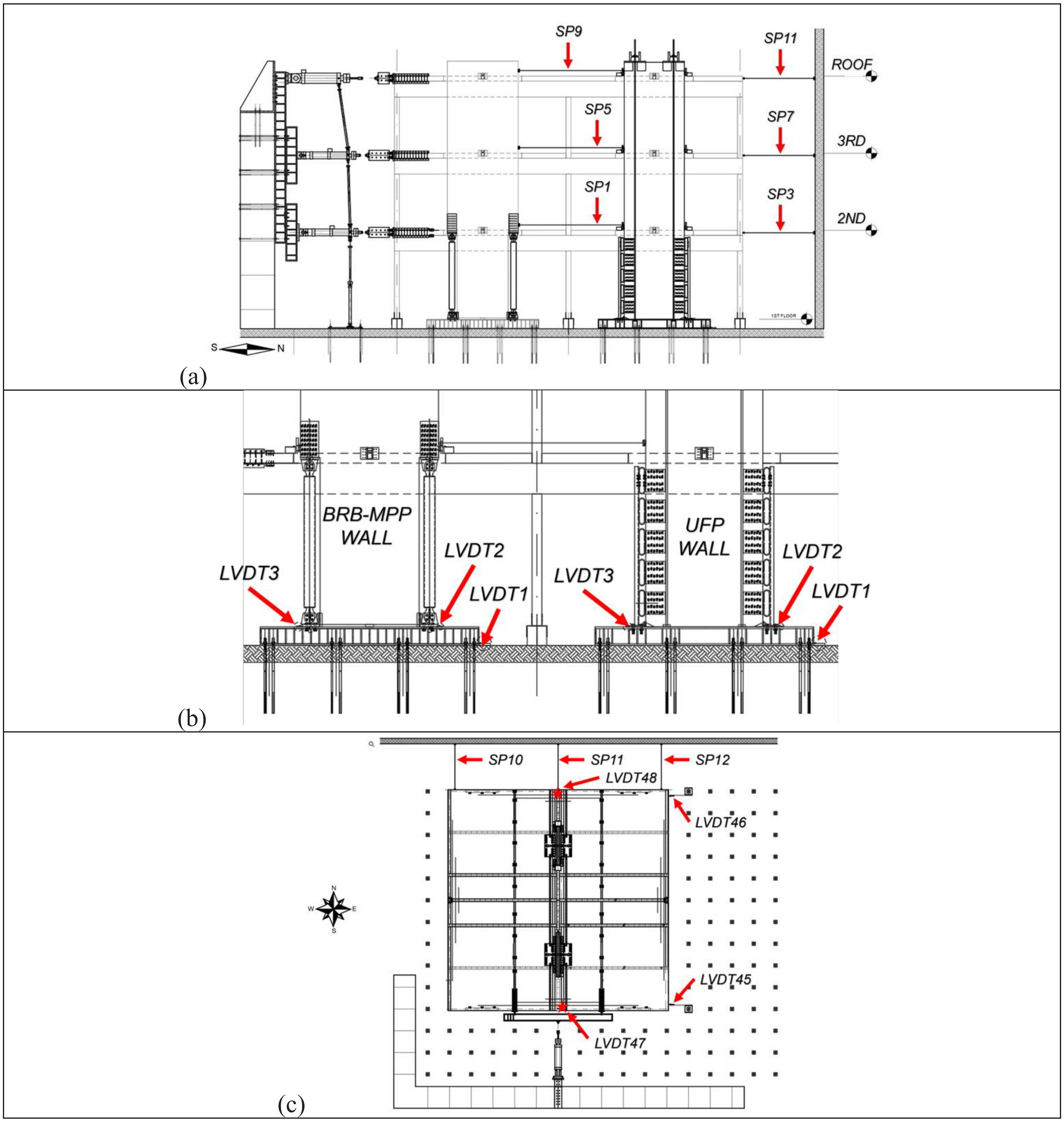

Figure 6. Instrumentation arrangements for observation of global building behavior: (a) string potentiometers for story and wall displacement; (b) LVDTs measuring beam foundation and wall sliding; and (c) string potentiometers LVDTs measuring torsion and out-of-plane movement at the roof.

the in-plane movement of the walls. At the ground level, three LVDTs were arranged to measure potential sliding movement of the steel foundation beam and two foundation shear keys (Figure 6b). Note that the same sensor IDs were used for Phase 1 and Phase 2.

At each floor level, there were three string potentiometers attached to diaphragm ends at the north side of the building to monitor the building displacements and potential building torsion and relative diaphragm movements on the north face. On the other hand, there were two LVDTs installed at the northeast and southeast corners of the diaphragm. Figure 6c shows the roof sensors as example of the setup.

The experiment involved tracking various aspects of the diaphragm's performance during the lateral movement of the building, under the double cantilever scenario (N-S direction). A pair of LVDTs on each floor were used to measure the opening of the diaphragms near the ends. Figure 6c shows the roof setup for this purpose (LVDT47 and LVDT48). Additionally, LVDTs were used to measure relative movement of the wing-plate to the MPP and relative movement of the tongue plate to wing plate, while strain gauges were used to measure strains in steel components, such as collectors and tongue plates. Figure 7 shows the reference location of the LVDTs at the roof. Detailed instrumentation drawings can be accessed in DesignSafe (Sinha et al. 2024, 2025).

Table 1 summarizes the instrumentation used during the testing program across the four phases. The table lists the sensor types, quantities, general locations, testing phases in which they were deployed, and a general description of the measurements they captured. LVDTs were primarily used to monitor local and global displacements of wall panels, diaphragms, and foundation components. String potentiometers captured in-plane wall movements and global floor displacements, while strain gauges measured axial strains in BRBs, PT rods, and diaphragms. The table highlights the comprehensive coverage of both local and global structural responses, ensuring that the behavior of critical elements was accurately recorded throughout the experimental program.

Additional instrumentation for BRB-MPP spine

The instrumentation at the base of the MPP spine consisted of two LVDTs at both sides of the MPP boundaries and one LVDT at the pivot support to measure uplift resulting from the tilting-mode behavior of the spine. LDVTs were also used to measure the axial deformation of the BRBs (two per BRB) and local deformations in the connections (four per BRB). Four strain gauges were installed in the elastic regions of each BRB (two on each face) and in the pivot-support rods (one per rod) to estimate axial forces in these elements. Other LVDTs not

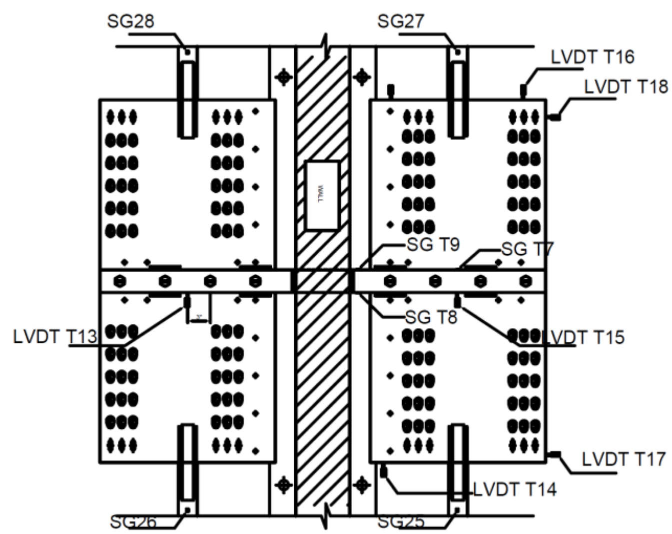

Figure 7. Wing and tongue plates instrumentation for roof.

Table 1. Instrumentation summary.

	Total quantity	Location	Phases(s) used	Measurement
LVDT	23	BRB wall	1	Local response at BRBs, wall panel, connections, and relative to diaphragm
	23	MPP wall	2	Local responses at the wall panel, UPFs, and relative to diaphragm
	6	Diaphragm-to-wall	1 and 2	Relative horizontal wall panel to diaphragm
	3	Foundation beam	1 and 2	Sliding
	6	Diaphragm	All	Global out-of-plane displacement
	30	Diaphragm	All	Local responses at the splines, collar beams, and shear key-to-wing plate
String pot	3	Wall-to-wall	1 and 2	In-plane wall displacement at floor levels
	9	Diaphragm	All	Global floor displacement
Strain gauges	8	BRB wall	1	BRB strains
	8	PT rods	2	PT rod strains
	24	Diaphragms	All	Strain at shear collector

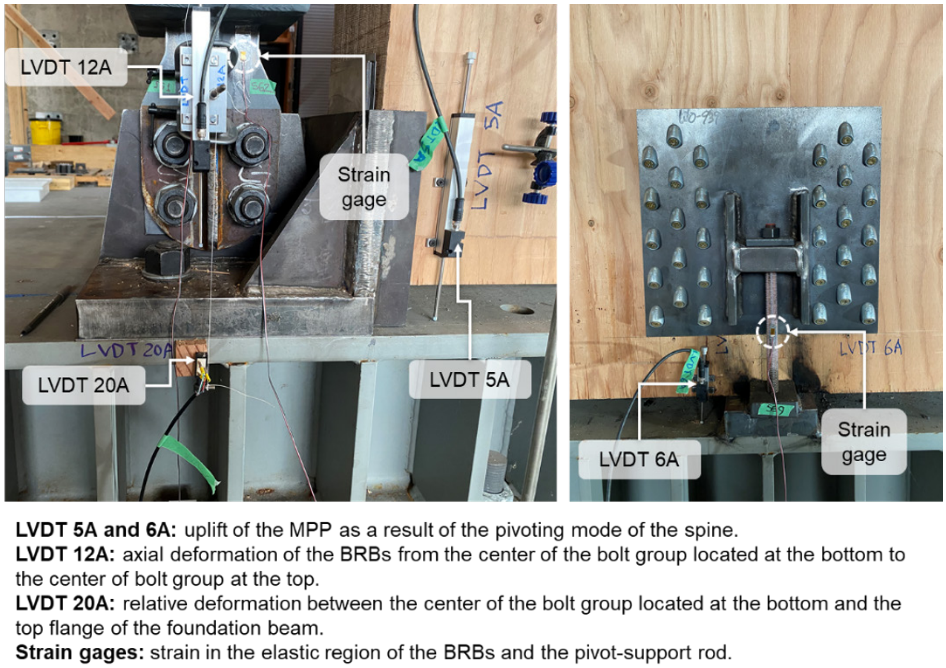

Figure 8. Instrumentation arrangements for pivoting wall.

shown in Figure 8 were installed at the base to measure lateral slip of the foundation beam and out-of-plane displacements at the base of the MPP spine.

Additional instrumentation for post-tensioned UFP wall

At the bottom interface of the rocking wall, there were seven LVDTs on the east face (Figure 9) and two LVDTs on the west face of the wall to measure the uplift movements. The data were utilized to determine the contact length of the rocking interface and helped to validate the design calculations. In addition, on each steel column, there was one LVDT to measure the relative vertical displacement between two branches of a UFP (Figure 9) and another LVDT to observe the gap opening between the steel column and the rocking wall at the top end of the column (Figure 9). In order to determine the tension forces in high-strength rods, two strain gauges were installed on the two opposite sides of each PT rod in the axial direction (Figure 9).

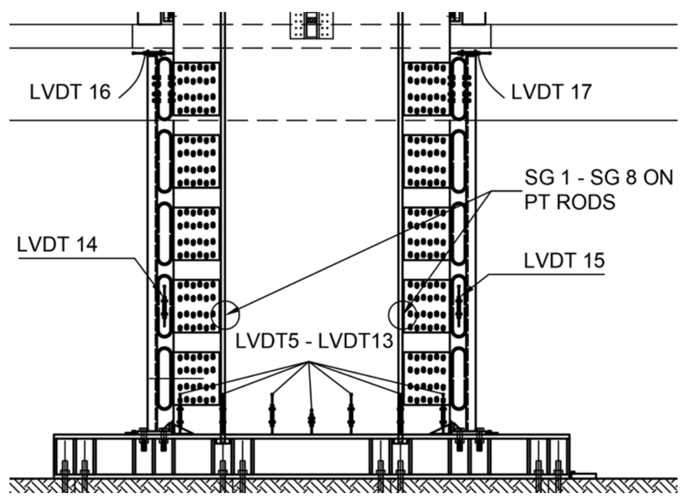

Figure 9. Instrumentation for rocking wall: (a) LVDTs at won East face, LVDT14 and LVDT15 measuring vertical UFP deformation, LVDT16 and LVDT17 measuring gap opening between steel column and wall panel, and strain gauges on high-strength rods.

Test phases

In addition to the two main phases (Phase 1 and Phase 2) in the test program of the building, there were two preceding tests, Phases 0.1 and 0.2, that were performed to characterize the stiffness of the gravity system. Thus, in Phase 0.1, the shear walls were not connected to the diaphragm; the primary actuator at the roof imposed the displacement following the modified CUREE protocol up to the 0.84% drift level, corresponding to 72 mm (2.8 in.) to avoid any possibility in damaging the gravity system. The purpose of this stage of testing was to determine the initial stiffness of the building gravity system and the contribution of the gravity system to the overall overstrength relative to the tested walls. In Phases 1 and 2, the pivoting BRB wall and post-tensioned UFP wall, respectively, were connected to the diaphragm through the shear key system at each floor level. The full loading protocol (up to 4% roof drift) was applied for the primary actuator in both phases to examine the structural performance of each LFRS, as well as the building as a complete system. Similarly, Phase 0.2 was conducted after completion of Phases 1 and 2, with the shear walls again left disconnected from the diaphragms. In this stage, the roof actuator pushed the building to a 2% drift to assess whether any degradation had occurred in the gravity system during the main testing phases.

Results and discussion

Gravity system contribution

The gravity system was subjected to displacement cycles reaching up to 0.84% drift of the loading protocol in Phase 0.1. The total base shear was calculated as the summation of forces from the three actuators. Figure 10a shows the base shear versus roof drift ratio hysteresis of the gravity system tested in Phase 0.1, while Figure 10b shows the hysteresis of the gravity system in Phase 0.2. A small positive shift in the base shear at the beginning of the second gravity-only test (approximately 1% of the specimen weight) reflects the need to re-zero the actuator based on the residual position from the preceding phase. Apart from this offset, the hysteresis responses from both tests showed no evidence of cyclic degradation. The peak base shears were 39.1 kN (8.8 kips) at 1% roof drift in the initial test and 46.7 kN (10.5 kips) at 2% roof drift in the final test. As expected for a system consisting solely of the gravity framing, only limited self-centering was observed.

The equivalent hysteretic damping of the gravity system per cycle was estimated after each cycle using the following equation:

$$\xi_{hyst,cycle} = \frac{1}{4\pi}\frac{E_{h,GS}}{E_{S0}} = \frac{1}{2\pi}\frac{E_{h,GS}}{V_{bt}\Delta_t} \quad [1]$$

where $E_{h,GS}$ is energy dissipated by the system in one complete cycle, E_{S0} is strain energy of the linear-elastic system at the target displacement, Δ_t, and base shear, V_{bt}, determined at the target displacement. The strain energy E_{S0} is the sum of the strain energy in positive and negative directions. Based on results in Phase 0.1, equivalent hysteretic damping of the gravity system per cycle increases from 0.049 to 0.075 with the increase of maximum roof drift ratio from 0.17% to 0.83%.

MPP pivoting wall

Performance

Figure 11a shows the total base shear-roof drift hysteretic behavior during Phase 1. The specimen maintained a nearly uniform distribution of story drift throughout the loading protocol, as intended. The building exhibited full and stable global hysteretic loops, including a complete cycle at the 4.0% enhanced-performance drift target and two subsequent cycles at 3.0%, without loss of lateral strength. The global response resembled other pivoting lateral systems supplemented primarily with BRBs, such as steel strongback frames (Simpson and Mahin 2018).

The BRBs governed the inelastic global behavior, while the MPP wall, diaphragms, and gravity system remained essentially elastic. BRB yielding occurred nearly simultaneously in tension

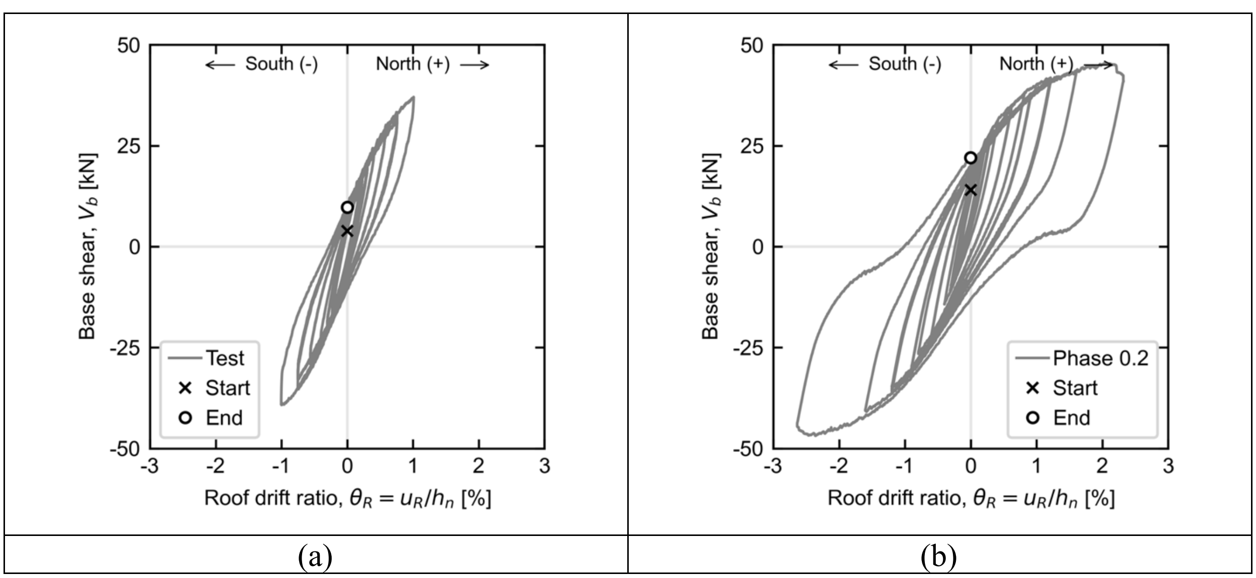

Figure 10. Cyclic behavior observed during: (a) Phase 0.1 and (b) Phase 0.2.

and compression at approximately 0.44% roof drift. As the BRBs yielded and strain-hardened, lateral strength increased, reaching a peak base shear V_b ≈ 222 kN, approximately twice the design base shear. At 4.0% roof drift, the system achieved a ductility demand of 9.09 relative to the drift at BRB yielding. The force-deformation loops maintained a stable, nearly symmetric shape throughout testing. Minor asymmetries between push and pull directions, particularly in trailing cycles, resulted from test setup and actuator load-transfer details, not from structural system behavior.

Figure 11b shows the estimated cyclic axial force-deformation behavior of the BRBs. After yielding, the BRBs exhibited the expected asymmetric kinematic and isotropic strain-hardening behavior, with similar axial deformations in tension and compression. At the 4.0% target drift, BRB deformations reached approximately 40 mm (1.57 in.), resulting in strains of near 2% in the yielding core, well within design criteria. The BRBs met all AISC 341 (AISC 2022) acceptance criteria for cyclic testing: (1) stable, repeatable behavior with positive incremental stiffness; (2) no rupture, instability, or connection failure; (3) maximum compression-to-tension force ratio below 1.50; and (4) cumulative inelastic axial deformation capacity (CPD) exceeding 200 times the yield deformation (measured CPD = 331). Low-cycle fatigue analyses indicated significant remaining BRB fatigue life at test completion (Araújo et al. 2025).

Equivalent hysteretic viscous damping was estimated from dissipated energy per cycle (Jacobsen 1960). In initial cycles, the hysteretic damping ratio remained relatively constant, around 0.06–0.07, associated with gravity system nonlinearity. After BRB yielding, damping increased to 0.32 at 2% roof drift and 0.41 at 4% drift, consistent with previous tests on systems employing BRBs as energy dissipators (Kim and Choi 2004; Sutcu et al. 2014; Zhu and Zhang 2008).

Residual drifts increased significantly after BRB yielding due to accumulated residual deformations, reaching 1.38% after unloading from 2.0% roof drift. While such residual drifts typically indicate significant repair costs, post-earthquake residual drifts are controlled by both cyclic behavior and ground motion characteristics and are generally less than quasi-static values measured in testing. For example, analytical estimates in Araújo et al. (2025), using an equivalent bilinear SDOF transformation (Kawashima et al. 1998; Macrae and Kawashimas 1997), suggested dynamic residual roof drift after the DE hazard level could be approximately 0.5% ± 0.3%.

Damage observations

Damage was concentrated in the BRBs in the form of permanent deformation, while all other components performed essentially elastically. Figure 12a shows initial state, while Figure 12b shows permanent deformation, and residual tilting near the gusset connection following testing. Permanent deformations in the yielding core appeared as the encased core protruding from the steel casing. Minor bending and superficial flaking developed at BRB end regions adjacent to bolted gusset plates, but did not affect hysteretic behavior. No brace-end fracture,

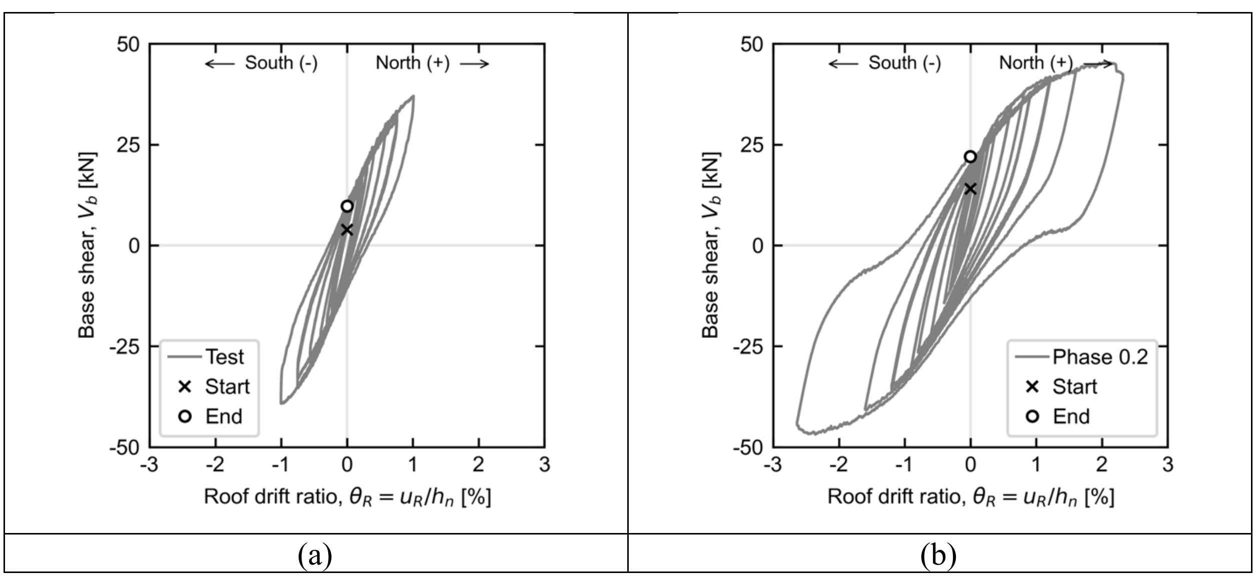

(a) (b)

Figure 11. Cyclic behavior observed during Phase 1: (a) global base shear-roof drift ratio; (b) local BRB force-axial deformation.

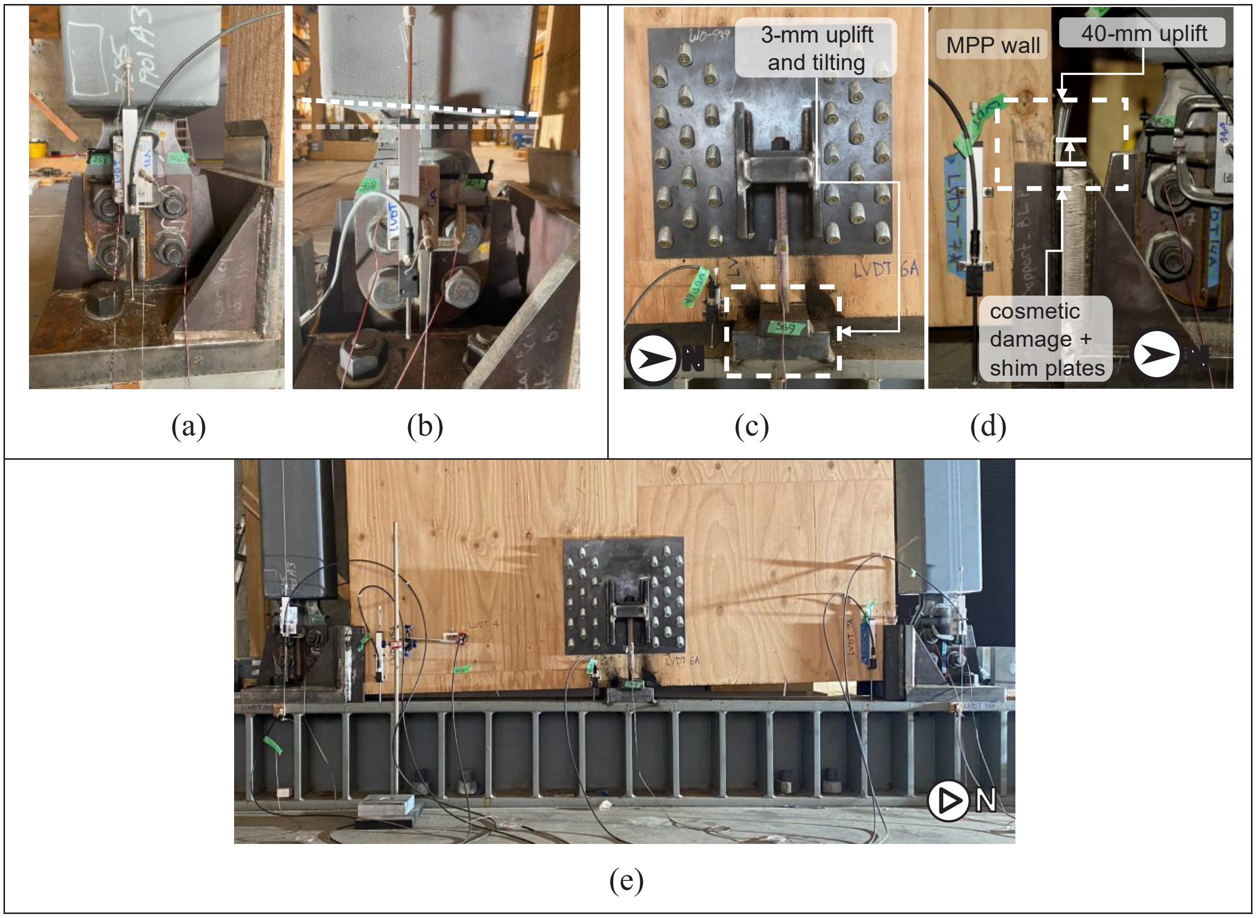

Figure 12. Damage observed in Phase 1: (a) permanent tilting of the wall at the end of the test; (b) uplift and tilting in pivoting support; (c) bearing marks in the wall toe; (d) bearing marks developed at base shear key interface; (e) final state of BRB walls at test completion depicting the residual drift.

buckling, or instability occurred throughout the protocol. Due to inelastic BRB deformations, the pivoting wall-BRB system remained tilted northward, with a residual roof drift of 2.25% at test completion; see Figure 12e.

The pivoting wall behaved as intended, with the MPP panel remaining essentially undamaged above the pivoting base. The pivot support enforced compatible, nearly symmetrical vertical deformation in both BRBs and limited wall uplift to a few millimeters; see Figure 12c. The wall base gap prevented concentrated compression zones at the wall toe, eliminating the crushing that often governs rocking-wall system performance. Only small, cosmetic bearing marks developed at base shear key interfaces, as shown in Figure 12d. Bearing damage in the MPP minor-strength direction was nearly negligible due to the sacrificial shim plates between the wall and shear key that distributed bearing stresses and accommodated rotation compatibility.

Post-tensioned MPP rocking wall

Performance

Figure 13a shows base shear versus roof drift ratio hysteresis for this test phase. The structure reached a base shear of 533.88 kN (120.02 kip) at 4.05% roof drift level and 520.98 kN (117.12 kip) at -3.59% drift level. Comparing with performance requirements, the building met all design requirement at the three design levels. All PT rods remained in the linear elastic range at performance levels 1 and 2 and exceeded the elastic limit strain at performance level 3.

Figure 13b shows the average PT force in the pairs of rods at north and south sides of the rocking wall. The average initial PT forces in the north and south pairs were 157.8 kN and 155.5 kN, respectively. When the building moved towards the north direction, the average PT force in the south pair increased up to 624.3 kN, primarily due to the rocking of the wall, which

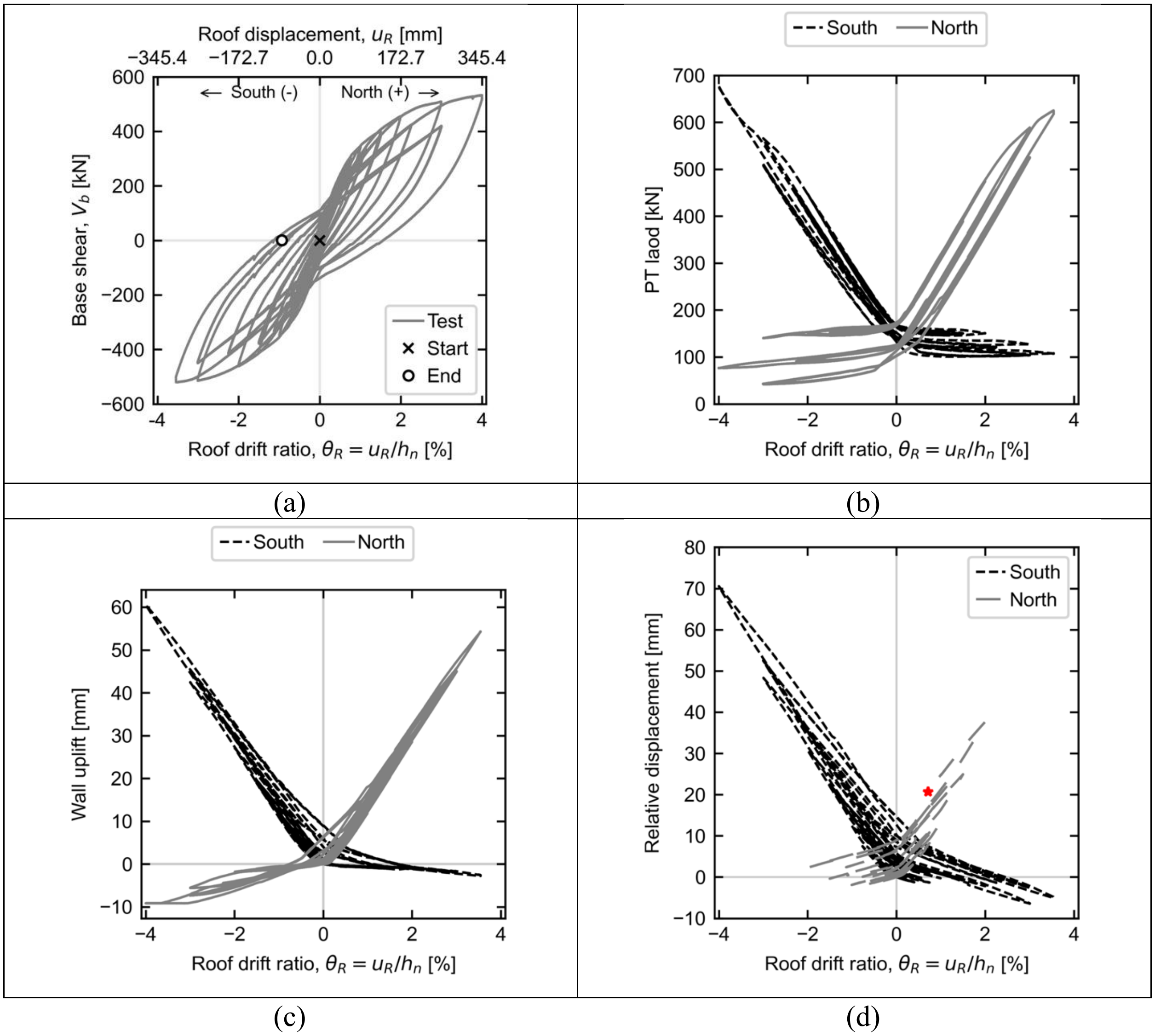

Figure 13. Cyclic behavior observed during Phase 2: (a) global base shear-roof drift ratio; (b) average PT rod strain deformation; (c) uplift measurements at bottom wall corners; and (d) UFP vertical relative displacement between the wall panel and boundary steel section.

was clearly visible as the wall uplift at the south corner wall base (see Figure 13c). The average PT forces on the north rods decreased 17.9% (to 129.6kN) when the building reached the drift level of 2%. This reduction of forces was expected, as the panel rocking induced some compression in the wall, which led to shortening of the north pair of rods. After reaching 3% and 4% drift levels, the tensile forces in both north and south PT forces considerably decreased because of the yield in PT rods and crushing of the MPP panel at the ends of the wall panel that were in contact with the foundation as the wall rocked. At the end of the test, the average PT forces in the north rod pair dropped to 39.4 kN (a reduction of 25% from the initial value). At 4.05% drift, the south end reached an uplift of 61 mm (2.40 in.), and north end compressed up to 9 mm (0.35 in.).

Figure 13d presents the relative vertical displacements recorded from the UFP assemblies. The measurements indicate that UFPs on the south edge of the wall registered negative relative displacements, suggesting greater toe damage on the north side of the wall, which aligns with the negative displacements measured at the base on north side of the wall (Figure 13c). The red star in Figure 13d marks the last reliable data point before the sensor detached from its support.

The estimation of hysteretic damping was conducted using Equation (1), similarly as in Phase 0.1, and showed that the equivalent hysteric damping per cycle varied from 0.011 to 0.081. The equivalent hysteretic damping ratios of new peak cycles of 1%, 2%, 3%, and 4% were 0.036, 0.054, 0.073, and 0.081, respectively.

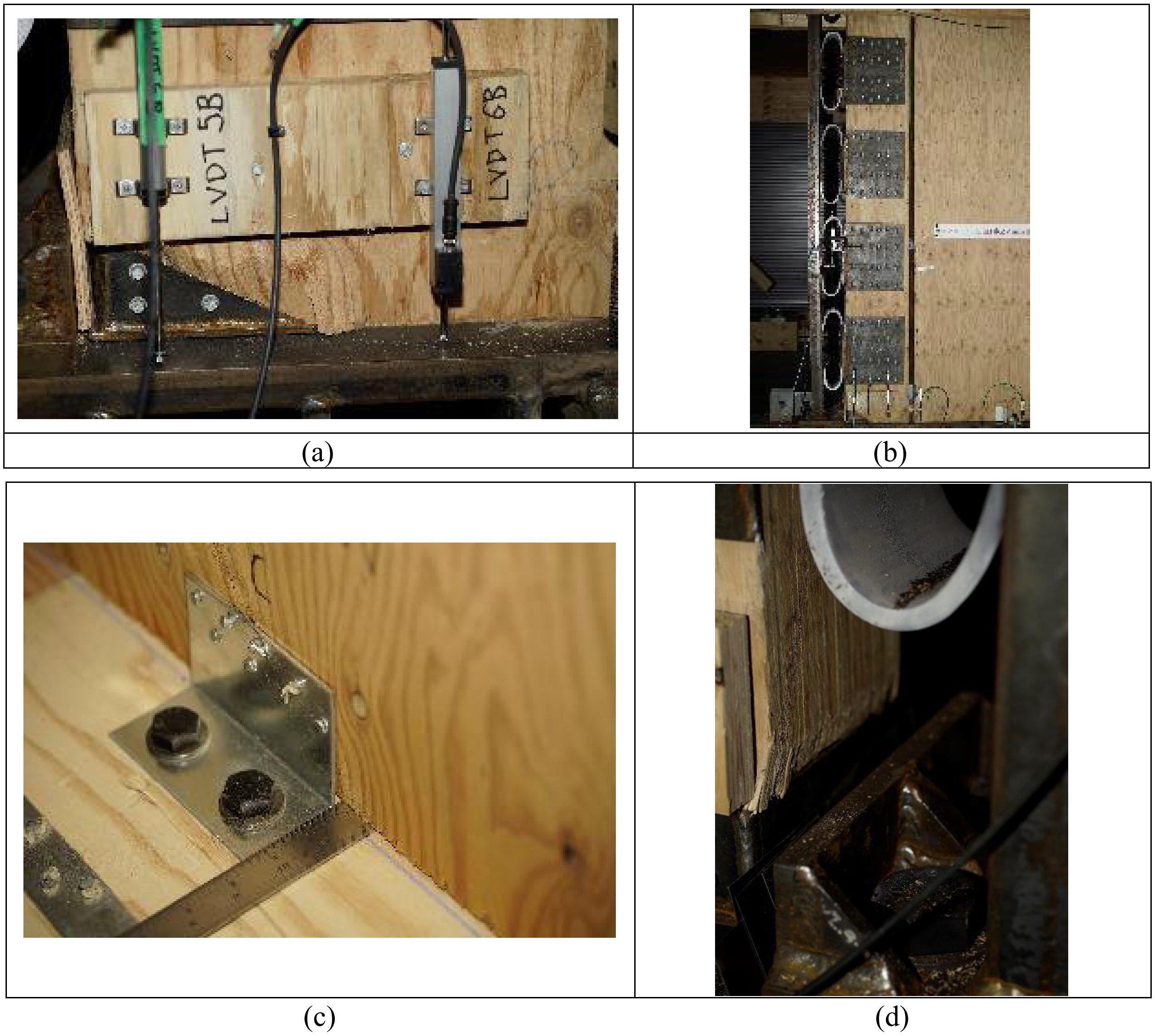

Figure 14. Damage observed in Phase 2: (a) Crushing at bottom corners of rocking panel; (b) deformation of steel side columns and UFPs; (c) nail damages and wall sliding at a bottom bracket connection between out of plane wall and diaphragm panels; and (d) mill scale at the bottom of the UFP.

Overall, the residual drift was less than or equal to 0.1%, 0.6%, and 1.7% at performance levels 1, 2, and 3, respectively. The results imply that the building experienced low-damage after the test, with permanent drift considerably lower.

Damage observation

There was no damage observed on the MPP rocking panel, especially at the area of rocking interface, at the 2% drift ratio level, which indicates that the panel was still in elastic range, as designed. After the 3% drift ratio level, crushing at the bottom corners of MPP panel (Figure 14a) was observed within a 200 mm (8 in.) wide and 80 mm (3 in.) high area from the vertical edge of the panel. Out of plane buckling of the exterior MPP layers along the edge of the steel toe was observed at the 3% drift ratio level. In addition, due to compression of the sacrificial plywood shims placed between the wall and the steel shoes, sliding of the wall started occurring, which induced the side steel columns to bend and the gap between side columns and vertical edges of MPP panel to increase, especially around the mid-span of the columns (Figure 14b). This mode of residual deformation kept increasing due to residual deformations of the steel column, the UFPs, or both.

Out of plane walls showed minor damage, including a few pull-out nails and broken nail heads at bracket connections, and wall sliding in the loading direction (Figure 14c) after the peak drift level of 4.05%. A maximum sliding of 7 mm (1/4 in.) was observed among out of plane walls after the test. Figure 14d shows steel mill scale aggregation deposited at the bottom of the UFPs as a sign of yielding in the UFPs.

The MPP diaphragms remained essentially elastic throughout the entire test. No visible signs of slip in the plywood splines or openings between the diaphragm panels were observed. Similarly, the beam-to-column connections in the gravity system were able to accommodate story drift demands up to 4% through rocking without inducing damage to the LVL columns. At such a drift level, sliding of the slotted plates in the gravity connections, relative to the LVL columns, was noticeable due to rocking.

Comparison between two systems

A direct comparison between the two LFRS highlights distinct seismic performance characteristics associated with each design philosophy. The BRB-MPP pivoting wall system exhibited stable and fuller hysteretic response with substantial energy dissipation capacity resulting from the yielding of the BRB. The system reached a peak base shear of approximately 222 kN, while maintaining stable cyclic behavior up to 4% roof drift without significant degradation in lateral resistance. Equivalent viscous damping increased substantially after BRB yielding, reaching values approaching 0.41 at large drift levels, indicating efficient hysteretic energy dissipation. However, the enhanced energy dissipation was accompanied by increased residual drift, due to permanent BRB deformations, with residual roof drift remaining at the completion of testing. In contrast, the post-tensioned rocking wall system developed significantly higher peak lateral resistance, exceeding 530 kN at approximately 4% roof drift, while exhibiting a flag-shaped hysteretic response characteristic of self-centering systems. Although the equivalent viscous damping ratios remained lower, reaching approximately 0.08 at the largest drift levels, the system demonstrated substantially improved recentering behavior and reduced residual drift demands, compared with the BRB-MPP system.

The observed damage mechanisms further demonstrate the fundamental behavioral differences between the two systems. In the BRB-MPP pivoting wall configuration, damage was intentionally concentrated within the BRBs through stable yielding and strain hardening, while the MPP wall, diaphragms, and gravity framing remained essentially elastic throughout the test program. The pivoting mechanism successfully prevented significant toe crushing and localized damage in the timber panel, thereby supporting the intended low-damage design philosophy. Conversely, the post-tensioned rocking wall system concentrated inelastic demands at the rocking interface and within the UFP energy dissipators. While the system maintained near-elastic behavior up to moderate drift levels and achieved an effective self-centering response, localized crushing at the wall toes, deformation of the boundary steel columns, and yielding of the UFP assemblies were observed at larger drift demands. Collectively, these results illustrate the inherent tradeoff between enhanced energy dissipation and residual deformation control. The BRB-based system provided superior hysteretic damping and energy absorption, whereas the post-tensioned rocking wall demonstrated improved recentering capability and reduced permanent deformation, both representing viable low-damage seismic design strategies for mass timber structures.

Conclusions

A three-story mass timber building was designed following a performance-based design methodology. The structure consists of MPP floor slabs, LVL beams and columns for the gravity framing, and two different LFRS solutions, including a MPP pivoting wall with BRB and post-tensioned MPP rocking walls with UFP energy dissipators.

1. The gravity framing, although not intended to participate in the LFRS, exhibited measurable lateral resistance and energy dissipation during testing. This unintended engagement contributed to system overstrength and enhanced damping at low drift ratios, highlighting the influence that gravity systems can have on the seismic response of self-centering mass-timber structures.
2. The hybrid spine combining a MPP wall with steel buckling-restrained braces (BRBs) provided effective lateral resistance: the BRBs yielded under cyclic loading, while the MPP wall remained largely elastic, allowing stable, repeatable hysteretic response with no evidence of cyclic degradation.
3. The capacity-designed connections and foundation shear-transfer assemblies used in the hybrid BRB-MPP spine demonstrated excellent robustness, maintaining structural integrity and stable behavior under drift demands that exceeded code-level earthquake intensities. This confirms that the system can reliably deliver enhanced seismic performance, while protecting the mass-timber components from inelastic damage.
4. The test results confirmed that the DDBD-based design approach for the mass-timber self-centering rocking wall provided reliable estimates of system response across the expected inelastic range. The methodology enabled controlled concentration of inelastic demands at the wall toes

and in the UFPs, while protecting the post-tensioning tendons and primary mass-timber components from significant damage. The system maintained near-zero residual drift up to moderate drift levels, and the measured equivalent viscous damping closely aligned with design predictions, demonstrating that simplified flag-shaped models can effectively represent the seismic behavior of self-centering systems with engaged gravity framing.

5. Cyclic testing of the three-story SCRW specimen showed that the wall achieved the intended rocking mechanism with stable performance up to 4% roof drift ratio. Inelastic demands remained localized, the PT rods stayed below yield-level strain, and the structure preserved its integrity despite minor residual drift and localized toe damage at large deformation levels. These results demonstrate that post-tensioned mass-timber rocking walls provide a robust, damage-controlled alternative for resilient seismic design.

Acknowledgements

The research project is funded by the United States Department of Agriculture (USDA), Agricultural Research Service, Award number: 58-2024-9-165 for the denominated Innovative Lateral Resisting Systems project. Additional support from USDA and the Tallwood Design Institute for capital building is greatly appreciated. Partial support by the National Science Foundation award number 2120683 is also acknowledged. The authors wish to express their appreciation for the generous support and donations provided by our industry partners, including Freres Engineered Wood, Boise Cascade, Simpson Strong-Tie, Fortis Construction, KPFF, Holmes, and the Portland Carpenters Union. The findings, opinions, recommendations, and conclusions in this paper are those of the authors and do not necessarily reflect the views of others, including the sponsors.

Special thanks are extended to Tanner Field, Steven Kontra, Kenneth Udele, Ian Morrell, Tyler Deboodt, and Kristian Walker from Oregon State University for their help with instrumentation and testing. The support provided by the TallWood Design Institute, particularly Byrne Miyamoto, Phil Mann, and Mark Gerig was essential throughout the experimental program. Acknowledgments are extended to Reid Zimmerman from KPFF Consulting Engineers, Eric McDonnell from Holmes, and Steve Pryor from Simpson Strong-Tie for their valuable feedback on the design of the lateral and gravity systems. Authors would like to acknowledge Steve Pryor's suggestion to perform lateral load testing of the gravity frame without connection to the vertical LFRS.

References

AISC (2022) Seismic provisions for structural steel buildings (ANSI/AISC 341-22). American Institute of Steel Construction. https://www.aisc.org/aisc/publications/current-standards/aisc-341/

Amini MO, van de Lindt JW, Rammer D, Pei S, Line P, Popovski M (2018) Systematic experimental investigation to support the development of seismic performance factors for cross laminated timber shear wall systems. Eng Struct 172:392–404. https://doi.org/10.1016/J.ENGSTRUCT.2018.06.021.

Araújo RGA, Simpson BG, Barbosa AR, Pieroni L, Ho TX, Orozco OGF, Miyamoto BT, Sinha A (2025) Experimental and numerical simulation of a three-story mass timber building with a pivoting wall and buckling-restrained boundary elements. J Struct Eng 151(7). https://doi.org/10.1061/JSENDH.STENG-13781.

ASCE/SEI (2017) Minimum Design Loads and Associated Criteria for Buildings and Other Structures. ASCE/SEI 7-16. American Society of Civil Engineers and Structural Engineering Institute, Reston, VA. https://ascelibrary.org/doi/pdf/10.1061/9780784414248.fm

ASTM (2017) Standard Specification for Quenched and Tempered Alloy Steel Bolts, Studs, and Other Externally Threaded Fasteners. A354-17e2. American Society for Testing and Materials (ASTM), West Conshohocken, PA. https://v1backup.astm.org/Standards/A354.htm

ASTM (2021) Standard Specification for High-Strength Low-Alloy Columbium-Vanadium Structural Steel. A572/A572M-21e1. American Society for Testing and Materials (ASTM), West Conshohocken, PA. https://store.astm.org/a0572_a0572m-21e01.html

ASTM (2025) Standard Specification for High Strength Structural Bolts and Assemblies, Steel and Alloy Steel, Heat Treated, Inch Dimensions 120 ksi, 144 ksi, and 150 ksi Minimum Tensile Strength, and Metric Dimensions 830 MPa and 1040 MPa Minimum Tensile Strength. F3125/F3125M. American Society for Testing and Materials (ASTM), West Conshohocken, PA. https://store.astm.org/f3125_f3125m-25.html

AWC/ANSI (2021) Special Design Provisions for Wind and Seismic (SDPWS). American Wood Council and American National Standards Institute, Leesburg, VA. https://awc.org/resources/2021-sdpws/

Barbosa AR, Rodrigues LG, Sinha A, Higgins C, Zimmerman RB, Breneman S, Pei S, van de Lindt JW, Berman J, McDonnell E (2021) "Shake-table experimental testing and performance of topped and untopped cross-laminated timber diaphragms." J Struct Eng 147(4). https://doi.org/10.1061/(ASCE)ST.1943-541X.0002914.

Blomgren H-E, Pei S, Jin Z, Powers J, Dolan JD, van de Lindt JW, Barbosa AR, Huang D (2019) "Full-scale shake table testing of cross-laminated timber rocking shear walls with replaceable components." J Struct Eng 145(10). https://doi.org/10.1061/(ASCE)ST.1943-541X.0002388.

Brown JR, Li M, Palermo A, Pampanin S, Sarti F (2021) Experimental testing of a low-damage post-tensioned C-shaped CLT core-wall. J Struct Eng 147(3). https://doi.org/10.1061/(ASCE)ST.1943-541X.0002926.

Di Cesare A, Ponzo FC, Pampanin S, Smith T, Nigro D, Lamarucciola N (2019) Displacement based design of post-tensioned timber framed buildings with dissipative rocking mechanism. Soil Dyn Earthq Eng 116:317–330. https://doi.org/10.1016/j.soildyn.2018.10.019.

Fernandez A, Komp J, Peronto J (2020) Ascent - challenges and advances of tall mass timber construction. Int J High-Rise Build 9(3):235–244. https://doi.org/10.21022/IJHRB.2020.9.3.235.

Ganey R, Berman J, Akbas T, Loftus S, Dolan JD, Sause R, Ricles J, Pei S, van de Lindt J, Blomgren H-E (2017) Experimental investigation of self-centering cross-laminated timber walls. J Struct Eng 143(10):4017135. https://doi.org/10.1061/(ASCE)ST.1943-541X.0001877.

Granello G, Palermo A, Pampanin S, Pei S, van de Lindt JW (2020) Pres-Lam buildings: State-of-the-art. J Struct Eng 146(6). https://doi.org/10.1061/(ASCE)ST.1943-541X.0002603.

IAPMO (2025) Simpson Strong-Tie Strong-Drive® SDW, SDWS, SDWH, and SDWV Screws. ESR-192.

ICC (2025) Simpson Strong-Tie® Strong-Drive Screws Used in Wood. ESR-3046.

ICC and APA (2025) VERSA-LAM® Laminated Veneer Lumber. ESR-1040.

Jacobsen LS (1960) "Damping in Composite Structures." 2nd World Conference on Earthquake Engineering. 2nd ed. Tokyo and Kyoto, Japan.

Kawashima K, Macrae GA, Hoshikuma J-I, Nagaya K (1998) Residual displacement response spectrum. J Struct Eng 124 (5):523–530. https://doi.org/10.1061/(ASCE)0733-9445(1998)124:5(523).

Kılınç AG (2025) Structural design of tall mass timber buildings. Athens J Technol Eng 12 (1):55. https://doi.org/10.30958/ajte.12-1-4.

Kim J, Choi H (2004) Behavior and design of structures with buckling-restrained braces. Eng Struct 26(6):693–706. https://doi.org/10.1016/J.ENGSTRUCT.2003.09.010.

Krawinkler H, Parisi F, Ibarra L, Ayoub A, Medina R (2000) Development of a Testing Protocol for Wood Frame Structures.

van de Lindt JW, Furley J, Amini MO, Pei S, Tamagnone G, Barbosa AR, Rammer D, Line P, Fragiacomo M, Popovski M (2019) Experimental seismic behavior of a two-story CLT platform building. Eng Struct 183:408–422. https://doi.org/10.1016/j.engstruct.2018.12.079.

Liven H, Abrahamsen R (2023) "Mjøstårnet: The world's tallest timber building." 13th World Conference on Timber Engineering, WCTE 2023, 7: 4209–4214. World Conference on Timber Engineering (WCTE), 19-22 June 2023, Oslo, Norway. https://doi.org/10.52202/069179-0547.

Macrae GA, Kawashimas K (1997) Post-earthquake residual displacement of bilinear oscillators. Earthq Eng Struct Dyn 26(7):701–716. https://doi.org/10.1002/(SICI)1096-9845(199707)26:7.

Mugabo I, Barbosa AR, Sinha A, Higgins C, Riggio M, Pei S, van de Lindt JW, Berman JW (2021) System identification of UCSD-NHERI shake-table test of two-story structure with cross-laminated timber rocking walls. J Struct Eng 147(4):1–17. https://doi.org/10.1061/(ASCE)ST.1943-541X.0002938 .

Nakaki SD, Stanton JF, Sritharan S (1999) An overview of the PRESSS five-story precast test building. PCI J 44(2):26–39. https://doi.org/10.15554/pcij.03011999.26.39.

Newcombe MP (2011) "Seismic design of post-tensioned timber frame and wall buildings." Ph.D. thesis, University of Canterbury.

Ocel JM, Provines J (2015) Properties of Anchor Rods Removed from San Francisco-Oakland Bay Bridge. US Dept of Transportation, Publication no. FHWA-HRT-15-057, Federal Highway Admin, McLean, VA. https://rosap.ntl.bts.gov/view/dot/35927

Palermo A, Pampanin S, Calvi GM (2004) Use of "controlled rocking" in the seismic design of bridges. Paper No. 4006, in 13th World Conference on Earthquake Engineering, August 1–6, 2004, Vancouver, BC, Canada. https://www.iitk.ac.in/nicee/wcee/article/13_4006.pdf

Pang W, Rosowsky DV, Pei S, van de Lindt JW (2010) Simplified direct displacement design of six-story woodframe building and pretest seismic performance assessment. J Struct Eng 136 (7):813–825. https://doi.org/10.1061/(ASCE)ST.1943-541X.0000181.

Pei S, van de Lindt JW, Barbosa AR, Berman JW, McDonnell E, Dolan JD, Blomgren H-E, Zimmerman RB, Huang D, Wichman S (2019) Experimental seismic response of a resilient 2-story mass-timber building with post-tensioned rocking walls. J Struct Eng 145(11):4019120. https://doi.org/10.1061/(ASCE)ST.1943-541X.0002382.

Pei S, Ryan KL, Berman JW, van de Lindt JW, Pryor S, Huang D, Wichman S, Busch A, Roser W, Wynn SL, Ji Y, Hutchinson T, Sorosh S, Zimmerman RB, Dolan J (2024) Shake-table testing of a full-scale 10-story resilient mass timber building. J Struct Eng 150(12). https://doi.org/10.1061/JSENDH.STENG-13752.

Priestley MJN, Calvi GM, Kowalsky MJ (2007) Displacement-Based Seismic Design of Structures. 1st Ed. Pavia, Italy: IUSS Press.

Priestley MJN, Grant DN (2005) Viscous damping in seismic design and analysis. J Earthq Eng 9(2):229–255. https://doi.org/10.1142/S1363246905002365.

Sarti F, Palermo A, Pampanin S (2015) Quasi-static cyclic testing of two-thirds scale unbonded posttensioned rocking dissipative timber walls. J Struct Eng 142(4). https://doi.org/10.1061/(ASCE)ST.1943-541X.0001291.

Sarti F, Palermo A, Pampanin S (2016) Development and testing of an alternative dissipative posttensioned rocking timber wall with boundary columns. J Struct Eng 142(4):E4015011. https://doi.org/10.1061/(ASCE)ST.1943-541X.0001390.

Simpson BG, Mahin SA (2018) Experimental and numerical investigation of strongback braced frame system to mitigate weak story behavior. J Struct Eng 144(2):04017211. https://doi.org/10.1061/(ASCE)ST.1943-541X.0001960.

Sinha A, Barbosa AR, Simpson BG, Araújo Rodriguez GA, Ho T, Orozco Orozco GF, Miyamoto B (2024) "Phase 1: Pivoting mass ply panel (MPP) wall and buckling-restrained boundary (BRB) elements in Emmerson Lab Launch Initiative (ELLI): Cyclic loading of a three-story building with lateral force resisting systems (LFRS) using mass timber products and steel energy dissipators." DesignSafe-CI. (2024). DesignSafe-CI. https://doi.org/10.17603/ds2-ec9j-ek15

Sinha A, Ho TX, Barbosa AR, Simpson BG, Uarac P PA, Orozco O GF (2025) "Phase 2: Mass ply panel (MPP) and U-shaped flexural plates (UFP) in Emmerson Lab Launch Initiative (ELLI): Cyclic loading of a three-story building with lateral force resisting systems (LFRS) using mass timber products and steel energy dissipators." DesignSafe-CI. https://doi.org/10.17603/ds2-p2jj-1j40

Soti R, Ho TX, Sinha A (2021) Structural performance characterization of mass plywood panels. J Mater Civ Eng 33(10). https://doi.org/10.1061/(ASCE)MT.1943-5533.0003902.

Sutcu F, Takeuchi T, Matsui R (2014) Seismic retrofit design method for RC buildings using buckling-restrained braces and steel frames. J Constr Steel Res 101:304–313. Elsevier. https://doi.org/10.1016/J.JCSR.2014.05.023.

Uarac PA, Ho TX, Barbosa AR, Simpson BG, Sinha A (2025) Design and cyclic testing of a full-scale three-story mass timber structure with post-tensioned self-centering rocking walls. J Build Eng 115:114505. https://doi.org/10.1016/j.jobe.2025.114505.

Zhu S, Zhang Y (2008) Seismic analysis of concentrically braced frame systems with self-centering friction damping braces. J Struct Eng 134(1):121–131. https://doi.org/10.1061/(ASCE)0733-9445(2008)134:1(121).